Title

Prediction of local fixed charge density loss in cartilage following ACL injury and reconstruction: A computational proof-of-concept study with MRI follow-up.

Journal

Journal of Orthopaedic Research, 39(5)

Authors

Orozco, Gustavo

Bolcos, Paul

Mohammadi, Ali

et al.

Publication Date

2021-05-01

DOI

10.1002/jor.24797

Peer reviewed

HHS Public Access

Author manuscript

J Orthop Res. Author manuscript; available in PMC 2022 May 01.

Published in final edited form as:

J Orthop Res. 2021 May ; 39(5): 1064–1081. doi:10.1002/jor.24797.

Prediction of local fixed charge density loss in cartilage following ACL injury and reconstruction: a computational proof-of-concept study with MRI follow-up

Gustavo A. Orozco[a,*], **Paul Bolcos**[a], **Ali Mohammadi**[a], **Matthew S. Tanaka**[b], **Mingrui Yang**[c], **Thomas M. Link**[b], **Benjamin Ma**[b], **Xiaojuan Li**[c], **Petri Tanska**[a], **Rami K. Korhonen**[a]

[a]Department of Applied Physics, University of Eastern Finland, Kuopio, Finland Yliopistonranta 1, FI-70210 Kuopio, Finland. [b]Department of Radiology and Biomedical Imaging, University of California, San Francisco, 1500 Owens St, San Francisco, CA 94158, USA. [c]Department of Biomedical Engineering, Lerner Research Institute, Program of Advanced Musculoskeletal Imaging (PAMI), 9500 Euclid Avenue, Cleveland Clinic, Cleveland, OH 44195, USA.

Abstract

The purpose of this proof-of-concept study was to develop 3D patient-specific mechanobiological knee joint models to simulate alterations in the fixed charged density (FCD) around cartilage lesions during the stance phase of the walking gait. Two patients with ACL reconstructed knees were imaged at 1- and 3-years after surgery. The MRI data was used for segmenting the knee geometries, including the cartilage lesions. Based on these geometries, finite element (FE) models were developed. The gait of the patients was obtained using a motion capture system. Musculoskeletal modeling was utilized to calculate knee joint contact and lower extremity muscle forces for the FE models. Finally, a cartilage adaptation algorithm was implemented in both FE models. In the algorithm, it was assumed that excessive maximum shear and deviatoric strains (calculated as the combination of principal strains), and fluid velocity, are responsible for the FCD loss. Changes in the longitudinal $T_{1\rho}$ and T_2 relaxation times were postulated to be related to changes in the cartilage composition and were compared with the numerical predictions. In Patient 1 model, both the excessive fluid velocity and strain caused the FCD loss primarily near the cartilage lesion. $T_{1\rho}$ and T_2 relaxation times increased during the follow-up in the same location. In contrast, in Patient 2 model, only the excessive fluid velocity led to a slight FCD loss near the lesion, where MRI parameters did not show evidence of alterations.

[*]Corresponding author: Gustavo A. Orozco, Department of Applied Physics, University of Eastern Finland, Kuopio, Finland, Yliopistonranta 1, 70210 Kuopio, FI, Tel: +358 50 3485018, gustavo.orozco@uef.fi.

Author Contributions: G.O. research design, acquisition, analysis, interpretation, manuscript drafting, and revision. P.B. acquisition, analysis, manuscript revision. A.L. acquisition, analysis, manuscript revision. M.T. acquisition, analysis, manuscript revision. M.Y. acquisition, analysis, manuscript revision. T.L. acquisition, analysis, manuscript revision. B.M. acquisition, research design, analysis, interpretation, manuscript drafting, and revision. X.L. research design, analysis, interpretation, manuscript drafting, and revision. P.T. research design, analysis, interpretation, manuscript drafting, and revision. R.K research design, analysis, interpretation, manuscript drafting, and revision. All authors have read and approved the final submitted manuscript.

Conflict of interest

The authors declare no potential conflict of interest.

Significance—This novel proof-of-concept study suggests mechanisms through which a local FCD loss might occur near cartilage lesions. In order to obtain statistical evidence for these findings, the method should be investigated with a larger cohort of subjects.

Graphical Abstract

A combination of MRI, gait analysis, musculoskeletal modeling, and mechanobiological FE modeling was utilized to simulate alterations in the FCD content around cartilage lesions during the stance phase in two patients with ACL reconstructed knees. Computational results were compared to the longitudinal changes observed in $T_{1\rho}$ and T_2 maps of MRI at 1- and 3-years after surgery. These predictions corresponded well with the findings of the $T_{1\rho}$ and T_2 relaxation times; they both increased during the follow-up around the defect where the model predicted FCD loss.

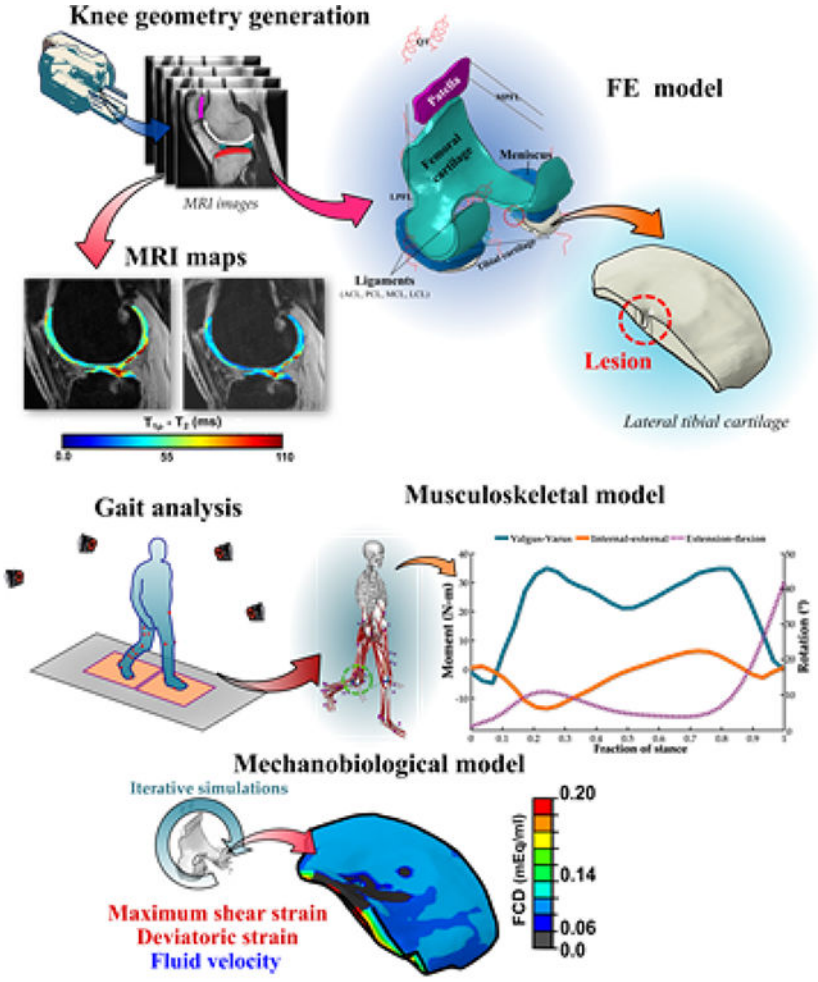

Keywords

Post-traumatic osteoarthritis; computational model; cartilage adaptation; finite element model; ACL reconstruction

Introduction

Anterior cruciate ligament (ACL) rupture is one of the most common traumatic knee joint injury which often involves damage to other tissues in the joint such as meniscus and cartilage. A rupture of the ACL mostly affects the young and healthy population causing not only pain and instability but it can also predispose the subject to post-traumatic osteoarthritis (PTOA).[1] Furthermore, there is a lack of evidence that ACL reconstruction is able to prevent the progression of PTOA.[2]

The signs of PTOA include a loss of fixed charge density (FCD) of proteoglycans (PGs) from cartilage and surface disruption with lesions penetrating into the tissue. Consequently, cartilage swelling decreases around the lesion, reducing the ability of the collagen network to support tensile forces. However, the local changes in the composition of cartilage associated with these physiological changes remain unclear and are challenging to predict.[3] If a method was available and it would be capable of predicting these tissue changes with time, planning future activities of patients and/or interventions would become both more straightforward and more effective.

It has been suggested that local cartilage lesions might contribute to the development of PTOA following an ACL injury and reconstruction.[4] Computational knee joint modeling has been used to predict changes in the properties of articular cartilage due to abnormal loading.[5] Likewise, *in vitro* mechanobiological models have been shown capable of simulating the FCD loss around cartilage lesions as a function of time.[6] Suggested mechanisms leading to PTOA have been related to higher localized tissue strains (shear, deviatoric) or fluid flow around the lesions, leading to FCD loss.[7] In fact, it has been suggested that **i)** FCD loss appears earlier than collagen damage[8,9] over a short follow-up time[10] and that **ii)** variations in the collagen fibril network organization are minor around cartilage defects.[11] Moreover, animal model studies have indicated that the collagen content does not change extensively in early PTOA, but rather follows other physical and compositional changes.[9,12] These findings form the basis for the analysis and prediction of cartilage FCD loss in injured joints. However, there are no studies that would have merged patient-specific knee joint models (including cartilage lesions) with adaptation algorithms in the quantitative and time-dependent prediction of cartilage FCD loss in ACL injured and reconstructed knee joints.

Recent magnetic resonance imaging (MRI) studies have revealed that $T_{1\rho}$ and T_2 relaxation times increase after the ACL injury and reconstruction surgery, suggesting that these are reflecting changes in cartilage composition.[13,14] However, there are no studies that have compared MRI follow-up information of ACL reconstructed patients with computational model predictions of FCD loss.

In this proof-of-concept investigation, we have applied an algorithm with **i)** maximum shear strain, **ii)** deviatoric strain, and **iii)** fluid velocity-controlled tissue adaptation mechanisms into 3D patient-specific fibril-reinforced poroviscoelastic knee joint finite element (FE) models with swelling properties. The models are used to simulate alterations in the FCD content around cartilage lesions during the stance phase of the gait. The numerical predictions emerging from the model are compared to the longitudinal changes in $T_{1\rho}$ and

T_2 relaxation times from MRI at 1- to 3-years after ACL reconstruction. We hypothesized that the localized change of the FCD content around cartilage lesions in the ACL reconstructed knees would correspond to the increases in the relaxation times. It was postulated that an estimation of these compositional changes with the mechanistic knee joint model could improve the identification of lesions at a high risk of progression to PTOA and could be applied for simulating surgical interventions and rehabilitation procedures. Thus, the model could ultimately suggest an optimal intervention to slow down or prevent the progression of PTOA.

Methods

Proof-of-concept-study workflow (Fig. 1)

Two patients with ACL reconstructed knees (*Patient 1*: 44 years, 79 kg; *Patient 2*: 39 years, 62 kg) were imaged at different follow-up time points using an MRI scanner (3.0T, MR750w, General Electric Healthcare). For both patients, full-thickness cartilage defects were diagnosed by 3 experienced musculoskeletal radiologists at baseline, however, meniscus injuries were not observed (see Supplementary material). A gait analysis was performed as these two patients were part of a larger longitudinal cohort in an NIH-funded study. The 1-year follow-up time point was used as an initial time point to predict FCD loss at the following time point (3-years) by combining MRI, gait analysis, musculoskeletal modeling, and a mechanobiological FE model. The 1-year time point was selected because by then, the gait patterns of the patients had become stabilized. Thereafter, the 1- and 3-year follow-up time points were used to monitor changes in cartilage composition from MRI findings. The subjects gave informed consent, and the data acquisition was permitted by and carried out in agreement with the rules and regulations of the Institutional Review Board (#11–06734) under the Human Research Protection Program at UCSF (Reference #: 187627).

Magnetic resonance imaging and analysis

Three-dimensional (3D) knee joint geometries were obtained within a 3D intermediate-weighted, fluid sensitive, fat-saturated fast-spin-echo MR image (CUBE).[15] The acquisition parameters were: repetition time (TR) = 1500 ms, echo time (TE) = 25 ms, field of view (FOV) = 16 cm, slice thickness = 1 mm, echo train length (ETL) = 32, matrix = 384×384, pixel size = 0.42 mm x 0.42 mm. Simultaneous acquisition of $T_{1\rho}$/T_2[16] was performed to quantify the $T_{1\rho}$ and T_2 relaxation times at the knee joint cartilage 1- and 3-years after surgery for both patients. Relaxation times were acquired using the following acquisition parameters for the MRI sequence: TR/TE= 9ms/min full, FOV= 14cm, matrix= 256×128, pixel size = 0.55 mm x 1.10 mm (0.55 mm x 0.55 mm with interpolation), slice thickness= 4mm, views per segment= 64, spin-lock frequency= 500 Hz, time of spin-lock = 0/10/40/80ms for $T_{1\rho}$ and preparation TE= 0/13.7/27.3/53.7ms for T_2.[17] Furthermore, the $T_{1\rho}$ and T_2 cartilage maps were computed on a pixel-by-pixel basis using a mono-exponential fit in Aedes (http://aedes.uef.fi) and in-house plugins for Matlab (R2017b, The MathWorks, Natick, MA, USA) (Fig. 1B). In addition, Whole-Organ Magnetic Resonance Imaging Scores (WORMS)[18] of the semi-quantitatively grade structural knee abnormalities

were obtained for the knees of both patients at 1- and 3-years after surgery; this is summarized in the Supplementary material.

Gait analysis and musculoskeletal modeling

The gait information of the patients was obtained at the 1-year follow-up time point using a published protocol.[19] The motion capture system consisted of 10 cameras (Vicon, Oxford metrics) and 41 retro-reflective markers to obtain segment position data. Simultaneously, two in-ground force plates (AMTI, Watertown, USA) were utilized to obtain the ground reaction forces. Then, a generic musculoskeletal model in OpenSim (SimTK, Stanford, CA, USA) was used to calculate knee joint contact and lower extremity muscle forces for the FE knee joint model.[20] The musculoskeletal model was composed of 12 body segments, 21 degrees of freedom and 92 muscle-tendon actuators. Anatomical landmarks collected during gait were used for scaling the generic model to the individual anthropometrics (i.e. segment lengths and masses) of both patients (Fig. 1C–D). The force of the quadriceps muscle was calculated as the sum of rectus femoris, vastus lateralis, vastus intermedius and vastus medialis. Knee joint and quadriceps forces were simulated for every trial. Then, the musculoskeletal model results were used to drive the knee joint FE models, similarly as has been done previously[21,22] (Fig. 2).

Finite element knee joint model

The acquired 3D CUBE MRI data at 1-year time point was used to segment the knee geometries (femoral, tibial, patellar cartilages, menisci, collateral, and cruciate ligament insertions), including the lesion/defect in the lateral tibial cartilage (*Patient 1:* depth=3.3 mm, diameter=~2.8 mm) and in the lateral femoral cartilage (*Patient 2:* depth=1.1 mm, diameter=~1.6 mm) (Fig. 3 and Supplemental Fig. S1), in Seg3D (v2.2.1, CIBC, Salt Lake City, UT, USA). To ensure the accuracy of the segmentation process, we consulted an experienced musculoskeletal radiologist (see acknowledgments). It is worth mentioning that the MRI data did not show any evidence of meniscal injuries in either patient, thus the menisci were modeled as being intact (see Supplementary material). Thereafter, the geometries were imported and meshed in Abaqus (v2018, Dassault Systèmes Simulia Corp., Providence, USA) where the FE models were constructed. Cartilages and menisci were meshed using 8-node hexahedral poroelastic (C3D8P) elements and modeled using fibril-reinforced poroviscoelastic and fibril-reinforced poroelastic materials, respectively, including swelling.[23] Specifically, the constitutive model assumes that the tissue is composed of solid and fluid matrices. The solid matrix is separated into a porous non-fibrillar part, representing the proteoglycan matrix, and a fibrillar network (viscoelastic in cartilage; elastic in meniscus), describing the collagen fibrils, and the influence of swelling caused by FCD. The total stress is given by

$$\boldsymbol{\sigma}_{\mathrm{tot}} = \boldsymbol{\sigma}_{\mathrm{s}} + \boldsymbol{\sigma}_{\mathrm{fl}} = \boldsymbol{\sigma}_{\mathrm{f}} + \boldsymbol{\sigma}_{\mathrm{nf}} - p\mathbf{I} - T_{\mathrm{c}}\mathbf{I} = \boldsymbol{\sigma}_{\mathrm{f}} + \boldsymbol{\sigma}_{\mathrm{nf}} - \Delta\pi\mathbf{I} - \mu^{\mathrm{f}}\mathbf{I} - T_{\mathrm{c}}\mathbf{I}, \quad (1)$$

where $\boldsymbol{\sigma}_{\mathrm{tot}}$ is the total stress tensor, $\boldsymbol{\sigma}_{\mathrm{s}}$ and $\boldsymbol{\sigma}_{\mathrm{fl}}$ represent the stress tensors of the solid and fluid matrices, respectively, p and $\Delta\boldsymbol{\pi}$ are the hydrostatic and swelling pressures, respectively, $\mathbf{I}$ is the unit tensor, μ^{f} is the chemical potential of water, T_{c} is the chemical expansion stress, and $\boldsymbol{\sigma}_{\mathrm{f}}$ and $\boldsymbol{\sigma}_{\mathrm{nf}}$ are the stress tensors of the fibrillar and non-fibrillar

matrices, respectively. A neo-Hookean material is utilized to define the non-fibrillar component, in which the stress tensor is given by

$$\boldsymbol{\sigma}_{\mathrm{nf}} = K_{\mathrm{nf}}\frac{\ln(J)}{J}\mathbf{I} + \frac{G_{\mathrm{nf}}}{J}\left(\mathbf{F}\cdot\mathbf{F}^{\mathrm{T}} - J^{\frac{2}{3}}\mathbf{I}\right), \tag{2}$$

where K_{nf} and G_{nf} are the bulk and the shear moduli of the non-fibrillar matrix and J is the determinant of the deformation gradient tensor $\mathbf{F}$. The bulk (K_{nf}) and shear (G_{nf}) modulus are established as

$$K_{\mathrm{nf}} = \frac{E_{\mathrm{nf}}}{3(1-2\nu_{\mathrm{nf}})}, \tag{3}$$

$$G_{\mathrm{nf}} = \frac{E_{\mathrm{nf}}}{2(1+\nu_{\mathrm{nf}})}, \tag{4}$$

where E_{nf} and ν_{nf} are the Young's modulus and the Poisson's ratio of the non-fibrillar matrix. The stresses in the viscoelastic collagen fibrils are defined with the damping coefficient η, the initial fibril network modulus E_0, and the strain-dependent fibril network modulus E_ε:

$$\sigma_{\mathrm{f}} = \begin{cases} -\dfrac{\eta}{2\sqrt{(\sigma_{\mathrm{f}} - E_0\varepsilon_{\mathrm{f}})E_\varepsilon}}\dot{\sigma}_{\mathrm{f}} + E_0\varepsilon_{\mathrm{f}} + \left(\dfrac{\eta E_0}{2\sqrt{(\sigma_{\mathrm{f}} - E_0\varepsilon_{\mathrm{f}})E_\varepsilon}} + \eta\right)\dot{\varepsilon}_{\mathrm{f}}, & \varepsilon_{\mathrm{f}} > 0 \\ 0, & \varepsilon_{\mathrm{f}} \le 0 \end{cases}, \tag{5}$$

while the stresses in the elastic collagen fibrils are given by

$$\sigma_{\mathrm{f}} = \begin{cases} E_{\mathrm{f}}\varepsilon_{\mathrm{f}}, & \varepsilon_{\mathrm{f}} > 0 \\ 0, & \varepsilon_{\mathrm{f}} \le 0 \end{cases}, \tag{6}$$

where σ_{f} and ε_{f} represent the fibril stress and strain, respectively. Therefore, collagen fibrils support primary tension. The fibril network stress emerges from the sum of primary and secondary collagen fibril stresses, which are computed individually for each integration point in each element.[23] Hence, stresses for these fibrils in tension are defined

$$\begin{cases} \sigma^{\mathrm{p}}_{\mathrm{f},i} = \rho_z C\sigma_{\mathrm{f}} \\ \sigma^{\mathrm{s}}_{\mathrm{f},i} = \rho_z\sigma_{\mathrm{f}} \end{cases}, \tag{7}$$

where $\sigma^{\mathrm{p}}_{\mathrm{f},i}$ and $\sigma^{\mathrm{s}}_{\mathrm{f},i}$ are the stresses for primary and secondary fibrils, respectively, ρ_z is the relative collagen density, and C is the density ratio between primary and secondary fibrils. Then, the total stress tensor of the fibrillar network is defined as the sum of the stresses in each individual fibril ($\sigma_{\mathrm{f},i}$):

$$\boldsymbol{\sigma}_{\mathrm{f}} = \sum_{i}^{totf} \sigma_{\mathrm{f},i} \overrightarrow{e}_{\mathrm{f},i} \otimes \overrightarrow{e}_{\mathrm{f},i} = \sum_{i}^{totf,\mathrm{p}} \sigma_{\mathrm{f},i}^{\mathrm{p}} \overrightarrow{e}_{\mathrm{f},i}^{\mathrm{p}} \otimes \overrightarrow{e}_{\mathrm{f},i}^{\mathrm{p}} + \sum_{i}^{totf,\mathrm{s}} \sigma_{\mathrm{f},i}^{\mathrm{s}} \overrightarrow{e}_{\mathrm{f},i}^{\mathrm{s}} \otimes \overrightarrow{e}_{\mathrm{f},i}^{\mathrm{s}}, \tag{8}$$

where *totf* is the total number of fibrils, $\overrightarrow{e}_{\mathrm{f},i}$ is the fibril orientation vector, *totf*, p and *totf*, s are the total number of primary and secondary fibrils, respectively, and $\overrightarrow{e}_{\mathrm{f},i}^{\mathrm{p}}$ and $\overrightarrow{e}_{\mathrm{f},i}^{\mathrm{s}}$ are the primary and secondary fibril orientation vectors, and ⊗ represents outer product. Furthermore, the Donnan osmotic swelling pressure at equilibrium is given by the equation

$$\Delta\pi = \phi_{\mathrm{int}} RT \left(\sqrt{c_{\mathrm{FCD}}^2 + 4\frac{\left(\gamma_{\mathrm{ext}}^{\pm}\right)^2}{\left(\gamma_{\mathrm{int}}^{\pm}\right)^2} c_{\mathrm{ext}}^2} \right) - 2\phi_{\mathrm{ext}} RT c_{\mathrm{ext}}\,, \tag{9}$$

where c_{FCD} is the fixed charge density content at equilibrium, c_{ext} is the external salt concentration (0.15 M), ϕ_{int} ϕ_{ext} $\gamma_{\mathrm{int}}^{\pm}$ and $\gamma_{\mathrm{ext}}^{\pm}$ are internal and external osmotic coefficients and internal and external activity coefficients, respectively, R is the molar gas constant (8.3145 J/mol K), and T is the absolute temperature (293 K). When temperature and external salt concentration are constant, then the only variable is the FCD which can be defined as a function of the tissue deformation, as

$$c_{\mathrm{FCD}} = c_{\mathrm{FCD}_0} \left(\frac{n_{\mathrm{fl}_0}}{n_{\mathrm{fl}_0} - 1 + J} \right), \tag{10}$$

where c_{FCD_0} is the initial fixed charge density and n_{fl_0} is the initial fluid volume fraction. Additionally, the chemical expansion stress T_{c} is determined as

$$T_{\mathrm{c}} = a_0 c_{\mathrm{FCD}} \exp\left(-\kappa \frac{\gamma_{\mathrm{ext}}^{\pm}}{\gamma_{\mathrm{int}}^{\pm}} \sqrt{c^{-}(c^{-} + c_{\mathrm{FCD}})} \right), \tag{11}$$

where a_0 and κ are material constants[23] and c^{-} is the mobile anion concentration. Moreover, the fluid flow in the non-fibrillar matrix is simulated according to Darcy's law:

$$q = -k\nabla p\,, \tag{12}$$

where q is the flux in the non-fibrillar matrix, ∇p is the hydrostatic pressure gradient vector across the region and k is the hydraulic permeability. The hydraulic permeability (k) is defined to be strain-dependent:

$$k = k_0 \left(\frac{e+1}{1+e_0} \right)^M = k_0 J^M, \tag{13}$$

where k_0 is the initial permeability, M is a positive constant, and e and e_0 are the current and initial void ratios, respectively.[24] The void ratio e is expressed by the ratio of the fluid to solid:

$$e = \frac{n_{\mathrm{fl}}}{n_{\mathrm{s}}}, \tag{14}$$

where n_{s} is the solid volume fraction and n_{fl} is the fluid volume fraction. The fluid velocity v_{fl} through the porous medium is established as

$$v_{\mathrm{fl}} = q\left(\frac{e+1}{e}\right) = -k\nabla p\left(\frac{e+1}{e}\right). \tag{15}$$

The depth-dependent primary collagen fibril orientations with split-line patterns, fluid fraction, and FCD distribution were implemented in the cartilage tissues.[25] In the menisci, the primary collagen fibrils were oriented circumferentially, and the fluid fraction and FCD content were homogeneously distributed. A complete list of the material parameters used is given in Table 1.

The meniscal roots were fixed to the bone using linear spring elements with the total stiffness of 350 N/mm at each root.[26] The quadriceps (QT) and patellar (PT) tendons, as well as collateral ligaments (MCL and LCL) and cruciate ligaments (ACL and PCL), were modeled using spring elements with a bilinear behavior.[27] These have recently been shown to provide reasonable FE modeling results, as compared to the models with solid ligaments.[28] The ligaments were assumed to be pre-elongated (MCL and LCL = 4%, ACL and PCL = 5%; of the initial length) at the segmented distance by using the bilinear spring option in Abaqus. The stiffness of the ligaments (MCL 100 N/mm, LCL 100 N/mm, ACL 380 N/mm, and PCL 200 N/mm,) and tendons (QT 475 N/mm and PT 545 N/mm) of the knee joint were selected from previous studies.[29,30] Similarly to previous studies[22,28], the springs were attached to the center of the anatomical attachment sites of each ligament and tendon, measured from MRI (Fig. 2). Ligament bottom anchorage points were fixed at the tibial bone sites during the gait cycle. The anchorage points at the femoral site were coupled to the main reference point (located at the midpoint between the condyles of the femur), allowing them to move along with the rigid bone. For PT, the bottom anchorage point was fixed at the tibial rigid bone while the top anchorage point was attached to the patellar bone. Likewise, the bottom anchorage point of the QT was fixed at the patellar bone while the tendon-muscle interface was defined by a reference point.

The following boundary conditions were applied to the mechanobiological knee joint models: bone was assumed as being rigid and the tibial cartilage-bone interface was fixed in all directions. Fluid flow was allowed only through the inner lesion surfaces (zero fluid pore). This approach has been implemented in previous studies.[7,21] Following an initial free-swelling step, the stance phase of the patient's gait obtained from the musculoskeletal model was implemented identically with earlier studies[22,28] (Fig. 2). In brief, the flexion-extension angle, and joint moments and translational forces during the stance phase of gait were computed and implemented to the main reference point. A time-dependent quadriceps force was applied to the tendon-muscle reference point (to apply the muscle force vector) which was coupled to the main reference point to follow the rigid bone motion.

Cartilage adaptation algorithm

A previously presented iterative adaptation algorithm was utilized to predict changes in the FCD content of cartilage.[7] This algorithm has been created to be closely dependent on three different model outputs: deviatoric and maximum shear strains, and interstitial fluid velocity, via Abaqus and Matlab. These outputs from the FE model were transferred to the algorithm, which assumed that FCD loss would occur in the aforementioned fibril-reinforced material model if either the deviatoric strain (ε_{dev}) exceeded a threshold of 20%, or the maximum shear strain (ε_{shr}) was greater than 40%, or the fluid velocity (v_{fl}) is larger than 0.03 mm/s during the entire stance phase of the gait cycle. The deviatoric strain can be defined by

$$\varepsilon_{dev} = \frac{1}{3}\left(\sqrt{(\varepsilon_1 - \varepsilon_2)^2 + (\varepsilon_1 - \varepsilon_3)^2 + (\varepsilon_2 - \varepsilon_3)^2}\right), \tag{16}$$

where ε_1, ε_2 and ε_3 are the principal strains. The maximum shear strain ε_{shr} is given by

$$\varepsilon_{shr} = max\{|\varepsilon_1 - \varepsilon_2|, |\varepsilon_1 - \varepsilon_3|, |\varepsilon_2 - \varepsilon_3|\} = |\varepsilon_{max} - \varepsilon_{min}|, \tag{17}$$

where ε_{max} and ε_{min} are the maximum and minimum principal strains, respectively.

The criteria regarding the strain thresholds were initially based on earlier studies.[6,31,32] A sensitivity analysis was also conducted (a strain threshold range was set from 0.15 to 0.6) to determine the correspondence between the simulation results and observed changes in the follow-up MRI maps. The initial fluid velocity threshold (0.03 mm/s) was chosen based on a previous study.[7] The sensitivity of the fluid velocity threshold to the modeling results was also tested (a threshold range was set from 0.01 to 0.2 mm/s). See the sensitivity analysis findings in the Results. We also tested diverse linear and nonlinear approaches to study the rate of FCD loss.[7] We obtained similar final homeostasis from each of them. Based on these assessments, we implemented a piece-wise constant adaptation rate factor D_r which can be defined as

$$D_r = \begin{cases} 0 & \text{if } \varepsilon_\beta < \varepsilon_{\beta,\,thres}, \\ 0.5 & \text{if } \varepsilon_{\beta,\,thres} \le \varepsilon_\beta \le \varepsilon_{\beta,\,breakdown} \\ 1 & \text{if } \varepsilon_\beta \ge \varepsilon_{\beta,\,breakdown}, \end{cases}, \quad \beta = \text{dev, shr} \tag{18}$$

where ε_β is the strain-variable (either deviatoric (β = dev) or maximum shear strain (β = shr)), $\varepsilon_{\beta,thres}$ is the strain threshold at which the cell death and the non-fibrillar matrix damage are assumed to initiate, indicated here by the FCD loss, and $\varepsilon_{\beta,breakdown}$ refers to an eventual breakdown of the ground substance after thousands of repetitions ($\varepsilon_{\beta,breakdown}$ = 1). For the case of the fluid velocity driven adaptation, a similar definition was utilized

$$D_r = \begin{cases} 0 & \text{if } v_{fl} < v_{fl,\,thres}, \\ 0.5 & \text{if } v_{fl,\,thres} \le v_{fl} \le v_{fl,\,breakdown} \\ 1 & \text{if } v_{fl} \ge v_{fl,\,breakdown}, \end{cases}, \tag{19}$$

where $v_{fl,thres}$ and $v_{fl,breakdown}$ are the fluid velocity values at which the non-fibrillar matrix damage is assumed to be initiated ($v_{fl,thres}$ = 0.03 mm/s) and an eventual breakdown occurs after thousands of repetitions ($v_{fl,breakdown}$ = 1.0 mm/s), respectively (Fig. 1E). The evolution of the non-fibrillar matrix damage can be reflected in the decreased FCD content via consecutive loading iterations (arbitrary time). The amount of FCD for each iteration i in the domain can be described as

$$c_{FCD_i} = c_{FCD_{i-1}} \cdot \left(1 - D_r\right), \tag{20}$$

following each iteration, the variation of the FCD content was implemented to modify the Donnan osmotic swelling pressure gradient and the chemical expansion stress (Eqs. 9 and 11), subsequently, the FCD decrease affects the total stress tensor (Eq. 1) in the forward iteration. The rate function (D_r) provided FCD loss predictions in a reasonable amount of time.

After the FE simulation of a patient's gait, an updated FCD content was obtained from the adaptation algorithm and was fed back to the FE model. This process was repeated 20 times (iterations) to predict possible changes in the FCD content as a function of time, which here refers to an arbitrary time. For computational stability purposes, the FCD content was not allowed to decrease to zero during the simulations. Hence, 10% of the initial FCD content was set as the smallest FCD concentration in the models. During the simulations, the FCD content distribution reached an equilibrium state, displaying a null FCD loss progression after iteration 16. The computational workflow of this proof-of-concept study is shown in Fig. 1.

Comparison between FCD loss predictions and MRI maps

The FCD loss predictions were contrasted with the changes observed in $T_{1\rho}$ and T_2 relaxation times of cartilage from 1- to 3-years after surgery; both qualitatively and quantitatively. In the quantitative analysis, volumes of FCD loss in the FE models and volumes of altered MRI signals were analyzed. In the FE models, volumes of elements associated with FCD loss were calculated from the last iteration, divided by the total volume of cartilage in each compartment. Using the MRI datasets, volumes of cartilage with $T_{1\rho}$ and T_2 relaxation times above 60 ms were calculated. This value is above the reported value in the literature (50 ms) for healthy cartilage[33] and the values between 50 and 60 ms were observed in the areas where the WORMS evaluation indicated healthy cartilage (see WORMS in Supplementary material). The relative volume of cartilage with altered relaxation times was calculated by subtracting the calculated volume at the 3-year time point from the volume at the 1-year time point, divided by the total volume of cartilage in the compartment. A sensitivity analysis of the effect of the relaxation time threshold on the results was also conducted (see more details in the Results).

Results

Sensitivity analysis for MRI relaxation time thresholds

The sensitivity analysis showed that when the relaxation time threshold was reduced from 60 ms to 50 ms, the volumes of cartilage with altered cartilage composition (as assumed from the altered MRI signal) reached the areas of healthy cartilage (based on WORMS evaluation included in Supplementary material) (Supplemental Figs. S2–S3).

Sensitivity analysis for adaptation algorithm thresholds

The sensitivity analysis for the numerical threshold values revealed that with smaller strain and fluid flow velocity threshold values, the FCD loss was faster and occurred also in other locations than those near to the cartilage lesions (e.g. deep cartilage and central tibial cartilage surface). In contrast, for larger values, the FCD loss was either prolonged or negligible in the entire cartilage volume (Supplemental Figs. S4–S5).

Patient-specific finite element models

For *Patient 1*, the FE model revealed those areas in the tibial cartilage where the maximum shear strain, deviatoric strain, and fluid velocity exceeded the thresholds of FCD loss and were at a maximum during the second peak of the stance phase (~0.75 stance fraction) (Fig. 4). For *Patient 2,* primarily the maximum shear strain exceeded the FCD loss threshold in small areas located in both the lateral and medial tibial cartilage during the first peak of the stance phase (~0.35 stance fraction) (Fig. 5). However, around the defect in the lateral femoral cartilage (Fig. 5C), only the fluid velocity exceeded the threshold in a small area during the loading response of the stance.

Qualitative and quantitative comparison between $T_{1\rho}$ and T_2 maps and mechanobiological model predictions

For *Patient 1*, volumes of $T_{1\rho}$ and T_2 relaxations times over the 60 ms threshold increased by ~18% and ~17% in the lateral tibial cartilage from 1- to 3-year follow-up time points, respectively (Figs. 6A and 7). These increases were specifically located near the lesion. The numerical predictions corresponded with the MRI findings and showed that the volume of FCD loss was ~9% near the lesion and located on the central surface of the lateral tibial cartilage when the FCD loss in the model was driven by the excessive maximum shear strain. With respect to the deviatoric strain criterion, the volume of FCD loss was 6.5%, while the fluid flow velocity mechanism predicted only ~2% FCD loss, particularly localized around the chondral lesion (Figs. 6B–D and 7). Smaller changes in the predicted FCD loss and altered MRI signals were observed in the medial joint compartment and patellar cartilage.

For *Patient 2*, the volumes of $T_{1\rho}$ and T_2 relaxation times over the 60 ms threshold increased by ~7% and ~2% in the medial and lateral tibial cartilages from the 1- to 3-year follow-up time points, respectively (Figs. 8A and 9). Numerical predictions were consistent with the MRI results and showed that the volume of FCD loss was 3.5% and 2% in the lateral and medial tibial cartilages, respectively when the model was driven by the maximum shear strain, while the deviatoric strain mechanism predicted a 0.5% FCD loss volume in the

lateral tibial cartilage. The FE model driven by the fluid flow velocity revealed a 0.2% FCD loss around the lesion in the femoral cartilage (Figs. 8B–D and 9).

Discussion

In the present proof-of-concept study, we applied a mechanobiological model to ACL reconstructed patients to predict the FCD loss in injured articular cartilage. The knee joint structures were segmented from MRI and the patient-specific motion was extracted from the combination of motion capture and a musculoskeletal model. Then, by utilizing a mechanobiological FE knee joint model, we predicted the FCD loss of injured cartilage under normal physiological loading (the stance phase of gait) by applying three different mechanisms to trigger PTOA (excessive fluid velocity, deviatoric strain, and maximum shear strain). Our mechanobiological model predictions corresponded well with the changes in the $T_{1\rho}$ and T_2 relaxation times obtained near the chondral lesion; they both either increased clearly during the follow-up at the same locations around the lesion where the model predicted an FCD loss or showed only minor or negligible increases. Numerical results suggested that both the fluid velocity and strain-based mechanisms could be plausible, though the maximum shear strain mechanism seems to explain better the cartilage FCD loss in the knee.

For *Patient 1*, the mechanobiological model driven by the strain-based mechanisms predicted a decrease in the FCD content near the lesion and on the surface of the lateral tibial cartilage, and a negligible FCD loss elsewhere. Localized FCD loss around the lesion was also predicted by the mechanobiological model driven by the fluid flow velocity. Consistently, elevated $T_{1\rho}$ and T_2 relaxation times and WORMS scores were observed during the follow-up, particularly in the lateral tibial cartilage at the site of the lesion, while fewer changes were observed elsewhere. In particular, the increased $T_{1\rho}$ relaxation time during the follow-up has been considered to be sensitive to FCD loss.[34,35] Our results were also in accordance with previous *in vivo* studies[36,37], computational models[21,38] and clinical evaluations[39,40] in which excessive strains have been suggested to contribute to cell death, matrix damage and FCD loss in injured cartilage.

For *Patient 2*, the slight or negligible increases observed in $T_{1\rho}$ and T_2 relaxation times and WORMS scores in the tibial cartilage during the follow-up support the numerical predictions of minor FCD loss. The model prediction showed the best correspondence with the experiments when the shear strain-driven mechanism was employed. Interestingly, the small FCD loss predicted by our mechanobiological model driven by the fluid flow velocity in the lateral femoral cartilage, including the defect, was in good agreement with the MRI follow-up data.

The findings from both models with different lesion sizes and anatomical locations are supported by previous studies that have reported the importance of location, shape, and size of lesions in determining the mechanical response of articular cartilage and risk for developing PTOA.[41] The clinical definition of critical lesion size for further structural changes of cartilage is 2.0 mm in diameter.[42] Based on this proof-of-concept study, the first model (*Patient 1*) includes a high-risk defect (diameter=~2.8 mm) as indicated by the

excessive shear strain-driven FCD loss. The second model (*Patient 2*) includes a low-risk lesion (diameter=~1.6 mm) for the development of PTOA, even though the excessive fluid velocity might explain the slight structural changes around the lesion. These results highlight the potential of utilizing these new mechanisms to categorize patients at high and low risk for the disease progression which may improve patient management and treatment.

Similar iterative tissue adaptation algorithms have been used for studying cartilage mechanics, bone remodeling, and tissue engineering approaches. The present investigation is the first to apply this approach using an entire knee joint model. The selection of the adaptation algorithm thresholds is crucial in our numeral approach. The proposed values were calculated from previous investigations and after many complementary simulations (sensitivity analysis), contrasting between the predictions from mechanobiological models and longitudinal changes in MRI maps. In concordance with our reported values, previous investigations have reported similar disruption thresholds[43] and failure strains.[44] Likewise, additional studies have defined similar fluid velocity values to describe mass transport processes and predict bone tissue formation in cartilage.

In this proof-of-concept study, some limitations exist regarding the clinical part, and numerical model development and specific assumptions. First, although two subjects might not represent all aspects of a population-based ACL reconstruction, it is a reasonable number for this proof-of-concept work, suggesting novel mechanisms to explain FCD loss. However, in future studies, more patients should be studied.

Second, the exact mechanical properties of cartilage and menisci of these patients were unknown, and their selection was based on previous studies.[28,38] Subject-specific material and compositional properties may affect the local strains and fluid velocities and, consequently, slightly change the predicted FCD loss. This was revealed recently in an *in vitro* computational model.[7] The predicted FCD loss might also change slightly if there were changes in material and compositional properties near the lesion immediately after the formation of the lesion. In addition, one might claim that the selection of healthy material parameters in the models is not accurate. However, WORMS gradings did not reveal any evident structural changes in different cartilage areas of the knee joint other than those close to the lesions. Nonetheless, if different material properties were used, they would neither change the observed mechanisms nor the conclusion of this study. Future numerical investigations might include the patient-specific properties of cartilage using quantitative MRI.[25,45]

Third, cartilage lesion geometries were segmented in a specific time and their propagation over time was not considered. However, the FCD decrease predictions concurred well with the follow-up MRI findings. In the future, defect propagation could be potentially included through a mesh-dependent damage theory which could account for nonlinear effects of mechanical loading on defect propagation in the tissue.[46] However, a validation of this approach would be challenging from MRI.

Fourth, we did not consider possible changes in the collagen network structure or content in our models because we assumed that the ground substance and the subsequent FCD loss

would appear prior to any disorganization of the collagen network, as has been reported before, particularly with a relatively short follow-up period.[7,10] A combined approach considering alterations in both collagen fibril network[11] and FCD after a traumatic knee joint injury will be a part of our future studies.

Fifth, our current model does not include a physical timescale (in days, months, years). Rather, an arbitrary time was considered, and 20 iterations used in our simulations could indicate thousands of repetitions. Our approach should be calibrated against *in vivo* and/or *in vitro* experiments in a time-dependent manner.

Sixth, the FCD content was not allowed to decrease to zero during the iterative process. The minimum value allowed was set to 10% of the smallest initial FCD content to avoid computational instabilities. The FCD distribution reached an equilibrium state after the iterative process. This might not be fully realistic since a possible further FCD loss might occur due to other factors that were not considered in the model, such as different physical activities, thresholds for the initiation of FCD loss, biochemically-driven degradation due to diffusion of inflammatory cytokines. However, our numerical predictions led to a good match with the experimental MRI follow-up data.

Due to the resolution of MRI, probably small uncertainties were present during the segmentation process. The voxel size was 0.55×0.55×4 mm which might mean that synovial fluid has contributed to the slightly increased relaxation times due to the partial volume effect, especially for *Patient 2*. However, since the changes were rather small, this uncertainty should not affect our conclusions.

For both patients, full-thickness cartilage lesions (WORMS score 2.5) were diagnosed at the 1-year follow-up time point by 3 experienced musculoskeletal radiologists. However, the cartilage lesions in both patients were challenging to identify and segment due to the size of the lesions and inherent limitations of MRI (i.e. the contrast between fluid and cartilage, spatial resolution). In particular, the lesion segmentation of *Patient 2* was challenging, and the final lesion geometry appears to be ideally symmetric. However, a musculoskeletal radiologist (see Acknowledgments) assisted us in identifying and segmenting the lesion geometries. It is also worth mentioning that our model predictions and $T_{1\rho}$ and T_2 relaxation times did not reveal any evidence of alterations around the lesion in *Patient 2*. Thus, even if the segmentation could be performed more accurately, the main conclusions would not change due to the small lesion size.

In conclusion, we suggest that the FCD decrease following ACL injury and reconstruction, including cartilage injury and subsequent tissue loading, might be caused by a large tissue deformation around the defect and extensive leakage of PGs through the damaged surface by high fluid outflow.[7] In the future, we will expand this proof-of-concept study to investigate also other mechanisms (biomechanical and biochemical) leading to changes in cartilage composition and structure after a traumatic joint injury, and compare the model results with the data obtained from a larger cohort of patients. After careful validation, the model could be applied in planning of joint loading and rehabilitation procedures to prevent or delay further disease progression.

Supplementary Material

Refer to Web version on PubMed Central for supplementary material.

Acknowledgments

The authors appreciate the support of the University of Eastern Finland, the University of California, San Francisco, and the Cleveland Clinic to undertake this study. CSC-IT Center for Science Ltd, Finland, is acknowledged for providing software resources. The experienced musculoskeletal radiologist Juha-Sampo Suomalainen, MD, is acknowledged for professional support. We acknowledge funding support from: The Doctoral Programme in Science, Technology and Computing (SCITECO), the European Union's Horizon 2020 research and innovation programme under the Marie Skłodowska-Curie grant agreement No 713645, Academy of Finland (grant no. 286526, 324529), Sigrid Juselius Foundation, Päivikki and Sakari Sohlberg Foundation, and from the National Institutes of Health (NIH/NIAMS; Grant P50 AR065645) and the American Orthopaedic Society of Sports Medicine (AOSSM) Genzyme Cartilage Initiative grant.

References

1. Øiestad BE, Engebretsen L, Storheim K, Risberg MA. 2009. Knee osteoarthritis after anterior cruciate ligament injury: a systematic review. Am J Sports Med 37(7):1434–1443. [PubMed: 19567666]
2. Brambilla L, Pulici L, Carimati G, et al. 2015. Prevalence of Associated Lesions in Anterior Cruciate Ligament Reconstruction: Correlation With Surgical Timing and With Patient Age, Sex, and Body Mass Index. Am J Sports Med 43(12):2966–2973. [PubMed: 26473010]
3. Trevino RL, Pacione CA, Malfait A-M, et al. 2017. Development of a Cartilage Shear-Damage Model to Investigate the Impact of Surface Injury on Chondrocytes and Extracellular Matrix Wear. Cartilage 8(4):444–455. [PubMed: 28934882]
4. Dulay GS, Cooper C, Dennison EM. 2015. Knee pain, knee injury, knee osteoarthritis & work. Best Pract Res Clin Rheumatol 29(3):454–461. [PubMed: 26612241]
5. Mononen ME, Liukkonen MK, Korhonen RK. 2019. Utilizing Atlas-Based Modeling to Predict Knee Joint Cartilage Degeneration: Data from the Osteoarthritis Initiative. Ann Biomed Eng 47(3):813–825. [PubMed: 30547410]
6. Eskelinen ASA, Mononen ME, Venäläinen MS, et al. 2019. Maximum shear strain-based algorithm can predict proteoglycan loss in damaged articular cartilage. Biomech Model Mechanobiol 18(3):753–778. [PubMed: 30631999]
7. Orozco GA, Tanska P, Florea C, et al. 2018. A novel mechanobiological model can predict how physiologically relevant dynamic loading causes proteoglycan loss in mechanically injured articular cartilage. Scientific Reports 8(1):15599. [PubMed: 30348953]
8. Mäkelä JTA, Rezaeian ZS, Mikkonen S, et al. 2014. Site-dependent changes in structure and function of lapine articular cartilage 4 weeks after anterior cruciate ligament transection. Osteoarthr. Cartil. 22(6):869–878.
9. Ronkainen AP, Tanska P, Fick JM, et al. 2019. Interrelationship of cartilage composition and chondrocyte mechanics after a partial meniscectomy in the rabbit knee joint - Experimental and numerical analysis. J Biomech 83:65–75. [PubMed: 30501912]
10. Hosseini SM, Veldink MB, Ito K, van Donkelaar CC. 2013. Is collagen fiber damage the cause of early softening in articular cartilage? Osteoarthr. Cartil. 21(1):136–143.
11. Tanska P, Julkunen P, Korhonen RK. 2018. A computational algorithm to simulate disorganization of collagen network in injured articular cartilage. Biomech Model Mechanobiol 17(3):689–699. [PubMed: 29177932]
12. Fick JM, Ronkainen P, Madden R, et al. 2016. Early in situ changes in chondrocyte biomechanical responses due to a partial meniscectomy in the lateral compartment of the mature rabbit knee joint. J Biomech 49(16):4057–4064. [PubMed: 27825604]
13. Pedoia V, Su F, Amano K, et al. 2017. Analysis of the articular cartilage T1ρ and T2 relaxation times changes after ACL reconstruction in injured and contralateral knees and relationships with bone shape. J. Orthop. Res. 35(3):707–717. [PubMed: 27557479]

14. Su F, Hilton JF, Nardo L, et al. 2013. Cartilage morphology and T1ρ and T2 quantification in ACL-reconstructed knees: a 2-year follow-up. Osteoarthritis and Cartilage 21(8):1058–1067. [PubMed: 23707754]
15. Teng H-L, Wu D, Su F, et al. 2017. Gait Characteristics Associated With a Greater Increase in Medial Knee Cartilage T1ρ and T2 Relaxation Times in Patients Undergoing Anterior Cruciate Ligament Reconstruction. Am J Sports Med 45(14):3262–3271. [PubMed: 28898105]
16. Li X, Pedoia V, Kumar D, et al. 2015. Cartilage T1ρ and T2 relaxation times: longitudinal reproducibility and variations using different coils, MR systems and sites. Osteoarthr. Cartil. 23(12):2214–2223.
17. Wang A, Pedoia V, Su F, et al. 2016. MR T1ρ and T2 of meniscus after acute anterior cruciate ligament injuries. Osteoarthr. Cartil. 24(4):631–639.
18. Peterfy CG, Guermazi A, Zaim S, et al. 2004. Whole-Organ Magnetic Resonance Imaging Score (WORMS) of the knee in osteoarthritis. Osteoarthr. Cartil. 12(3):177–190.
19. Samaan MA, Facchetti L, Pedoia V, et al. 2017. Cyclops lesions are associated with altered gait patterns and medial knee joint cartilage degeneration at 1 year after ACL-reconstruction. J. Orthop. Res. 35(10):2275–2281. [PubMed: 28128475]
20. Bolcos PO, Mononen ME, Mohammadi A, et al. 2018. Comparison between kinetic and kinetic-kinematic driven knee joint finite element models. Scientific Reports 8(1):17351. [PubMed: 30478347]
21. Venäläinen MS, Mononen ME, Salo J, et al. 2016. Quantitative Evaluation of the Mechanical Risks Caused by Focal Cartilage Defects in the Knee. Scientific Reports 6:37538. [PubMed: 27897156]
22. Halonen KS, Mononen ME, Jurvelin JS, et al. 2013. Importance of depth-wise distribution of collagen and proteoglycans in articular cartilage—A 3D finite element study of stresses and strains in human knee joint. Journal of Biomechanics 46(6):1184–1192. [PubMed: 23384762]
23. Wilson W, van Donkelaar CC, van Rietbergen B, Huiskes R. 2005. A fibril-reinforced poroviscoelastic swelling model for articular cartilage. J Biomech 38(6):1195–1204. [PubMed: 15863103]
24. Wilson W, van Donkelaar CC, van Rietbergen B, et al. 2004. Stresses in the local collagen network of articular cartilage: a poroviscoelastic fibril-reinforced finite element study. J Biomech 37(3):357–366. [PubMed: 14757455]
25. Räsänen LP, Tanska P, Zbýň Š, et al. 2017. The effect of fixed charge density and cartilage swelling on mechanics of knee joint cartilage during simulated gait. J Biomech 61:34–44. [PubMed: 28807526]
26. Villegas DF, Maes JA, Magee SD, Haut Donahue TL. 2007. Failure properties and strain distribution analysis of meniscal attachments. Journal of Biomechanics 40(12):2655–2662. [PubMed: 17359982]
27. Butler DL, Kay MD, Stouffer DC. 1986. Comparison of material properties in fascicle-bone units from human patellar tendon and knee ligaments. Journal of Biomechanics 19(6):425–432. [PubMed: 3745219]
28. Orozco GA, Tanska P, Mononen ME, et al. 2018. The effect of constitutive representations and structural constituents of ligaments on knee joint mechanics. Scientific Reports 8(1):2323. [PubMed: 29396466]
29. Gantoi FM, Brown MA, Shabana AA. 2013. Finite Element Modeling of the Contact Geometry and Deformation in Biomechanics Applications1. J. Comput. Nonlinear Dynam 8(4):041013–041013.
30. Mommersteeg TJA, Blankevoort L, Huiskes R, et al. 1995. The effect of variable relative insertion orientation of human knee bone-ligament-bone complexes on the tensile stiffness. Journal of Biomechanics 28(6):745–752. [PubMed: 7601874]
31. Hosseini SM, Wilson W, Ito K, van Donkelaar CC. 2014. A numerical model to study mechanically induced initiation and progression of damage in articular cartilage. Osteoarthritis and Cartilage 22(1):95–103. [PubMed: 24185112]
32. Zevenbergen L, Gsell W, Chan DD, et al. 2018. Functional assessment of strains around a full-thickness and critical sized articular cartilage defect under compressive loading using MRI. Osteoarthritis and Cartilage 26(12):1710–1721. [PubMed: 30195045]

33. Li X, Kuo D, Theologis A, et al. 2011. Cartilage in anterior cruciate ligament-reconstructed knees: MR imaging T1{rho} and T2--initial experience with 1-year follow-up. Radiology 258(2):505–514. [PubMed: 21177392]
34. Li X, Cheng J, Lin K, et al. 2011. Quantitative MRI using T1ρ and T2 in human osteoarthritic cartilage specimens: Correlation with biochemical measurements and histology. Magn Reson Imaging 29(3):324–334. [PubMed: 21130590]
35. Wheaton AJ, Casey FL, Gougoutas AJ, et al. 2004. Correlation of T1ρ with fixed charge density in cartilage. Journal of Magnetic Resonance Imaging 20(3):519–525. [PubMed: 15332262]
36. Gratz KR, Wong BL, Bae WC, Sah RL. 2008. The effects of focal articular defects on intra-tissue strains in the surrounding and opposing cartilage. Biorheology 45(3–4):193–207. [PubMed: 18836224]
37. Guettler JH, Demetropoulos CK, Yang KH, Jurist KA. 2004. Osteochondral defects in the human knee: influence of defect size on cartilage rim stress and load redistribution to surrounding cartilage. Am J Sports Med 32(6):1451–1458. [PubMed: 15310570]
38. Myller KAH, Korhonen RK, Töyräs J, et al. 2019. Computational evaluation of altered biomechanics related to articular cartilage lesions observed in vivo. J. Orthop. Res. 37(5):1042–1051. [PubMed: 30839123]
39. Shimizu T, Samaan MA, Tanaka MS, et al. 2019. Abnormal Biomechanics at 6 Months Are Associated With Cartilage Degeneration at 3 Years After Anterior Cruciate Ligament Reconstruction. Arthroscopy 35(2):511–520. [PubMed: 30473456]
40. Amano K, Huebner JL, Stabler TV, et al. 2018. Synovial Fluid Profile at the Time of Anterior Cruciate Ligament Reconstruction and Its Association With Cartilage Matrix Composition 3 Years After Surgery. Am J Sports Med 46(4):890–899. [PubMed: 29364702]
41. Gratz KR, Wong BL, Bae WC, Sah RL. 2009. The effects of focal articular defects on cartilage contact mechanics. J. Orthop. Res. 27(5):584–592. [PubMed: 18979528]
42. Salonius E, Rieppo L, Nissi MJ, et al. 2019. Critical-sized cartilage defects in the equine carpus. Connect. Tissue Res. 60(2):95–106. [PubMed: 29560747]
43. Párraga Quiroga JM, Wilson W, Ito K, van Donkelaar CC. 2017. The effect of loading rate on the development of early damage in articular cartilage. Biomech Model Mechanobiol 16(1):263–273. [PubMed: 27514541]
44. Men Y-T, Jiang Y-L, Chen L, et al. 2017. On mechanical mechanism of damage evolution in articular cartilage. Mater Sci Eng C Mater Biol Appl 78:79–87. [PubMed: 28576051]
45. Wan C, Ge L, Souza RB, et al. 2019. T1ρ-based fibril-reinforced poroviscoelastic constitutive relation of human articular cartilage using inverse finite element technology. Quant Imaging Med Surg 9(3):359–370. [PubMed: 31032184]
46. Sadeghi H, Lawless BM, Espino DM, Shepherd DET. 2018. Effect of frequency on crack growth in articular cartilage. J Mech Behav Biomed Mater 77:40–46. [PubMed: 28888932]
47. Julkunen P, Kiviranta P, Wilson W, et al. 2007. Characterization of articular cartilage by combining microscopic analysis with a fibril-reinforced finite-element model. Journal of Biomechanics 40(8):1862–1870. [PubMed: 17052722]
48. Saarakkala S, Julkunen P. 2010. Specificity of Fourier Transform Infrared (FTIR) Microspectroscopy to Estimate Depth-Wise Proteoglycan Content in Normal and Osteoarthritic Human Articular Cartilage. Cartilage 1(4):262–269. [PubMed: 26069557]
49. Dabiri Y, Li LP. 2013. Altered knee joint mechanics in simple compression associated with early cartilage degeneration. Comput Math Methods Med 2013:862903. [PubMed: 23424607]
50. Makris EA, Hadidi P, Athanasiou KA. 2011. The knee meniscus: Structure–function, pathophysiology, current repair techniques, and prospects for regeneration. Biomaterials 32(30):7411–7431. [PubMed: 21764438]
51. Mow VC, Ratcliffe A. 1997. Structure and Function of Articular Cartilage and Meniscus. Philadelphia, PA: Lippincott-Raven (2).

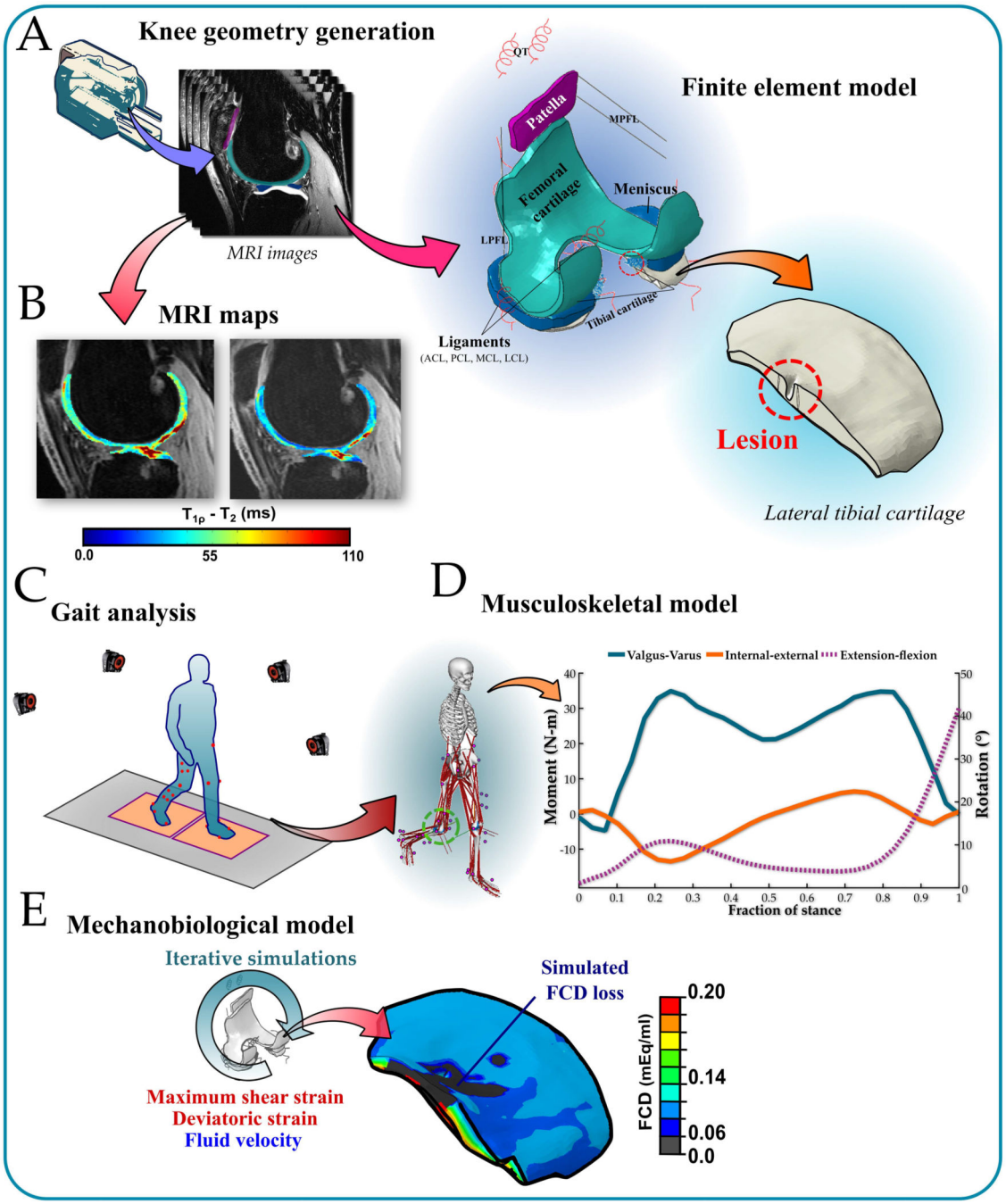

Figure 1.

(A) Segmentation of knee geometries for the finite element model. (B) Simultaneous MRI acquisition was performed to generate $T_{1\rho}$ and T_2 maps. (C) Gait data of both patients based on motion analysis. (D) Knee joint biomechanical data obtained from a musculoskeletal model. (E) Mechanobiological knee joint models driven by the adaptation algorithm by assuming that excessive maximum shear strain, deviatoric strain, and fluid velocity cause the FCD loss.

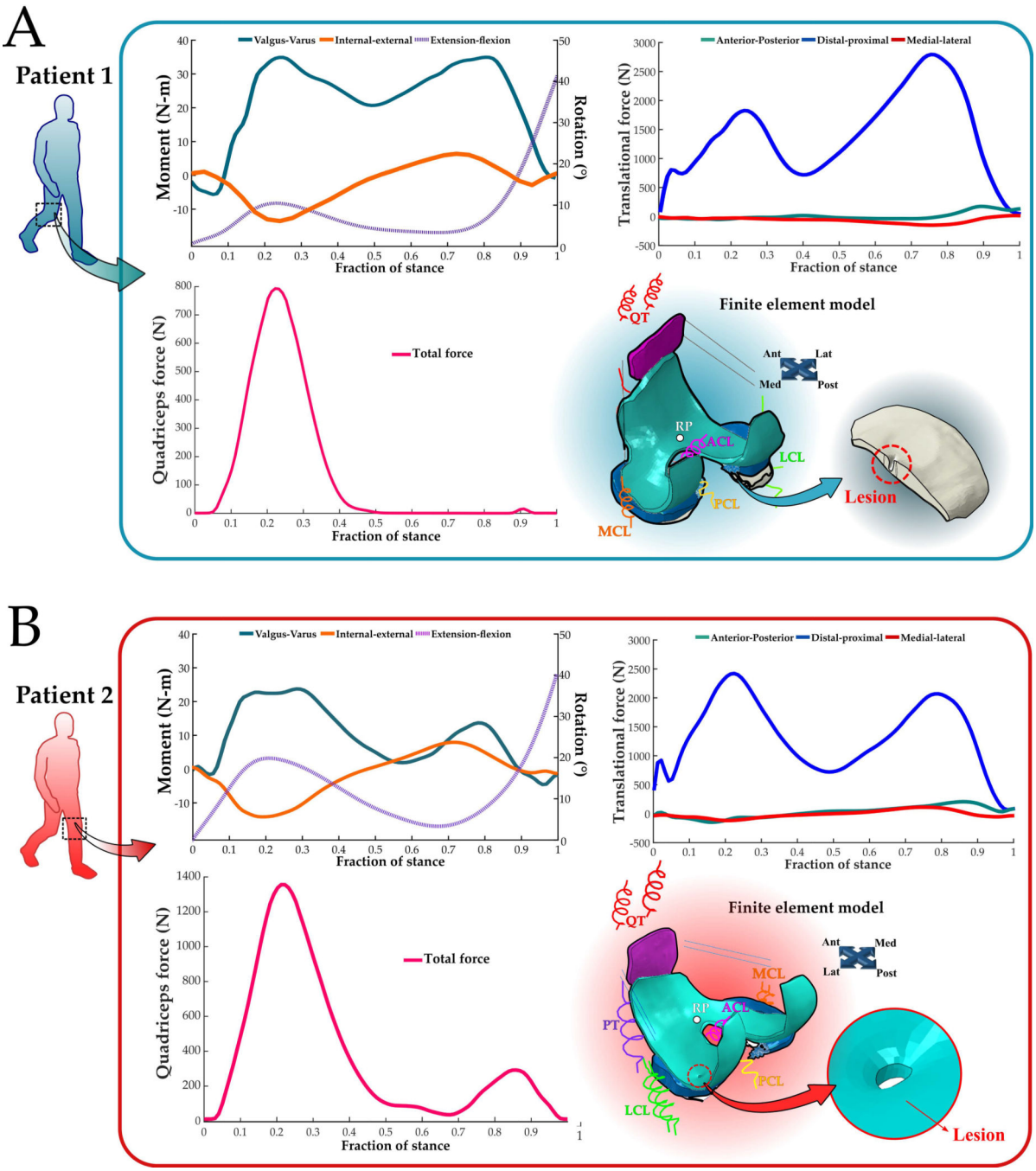

Figure 2.

Gait data for the computational knee joint model of both patients: External-internal and valgus-varus moments, and flexion-extension rotation. In addition, anterior-posterior, distal-proximal and medial-lateral forces, and total quadriceps force. Finally, a posterior-lateral view of the three-dimensional finite element model of the knee shows articular cartilages (including lesion), ligaments and tendons in *Patient 1* (A) and in *Patient 2* (B).

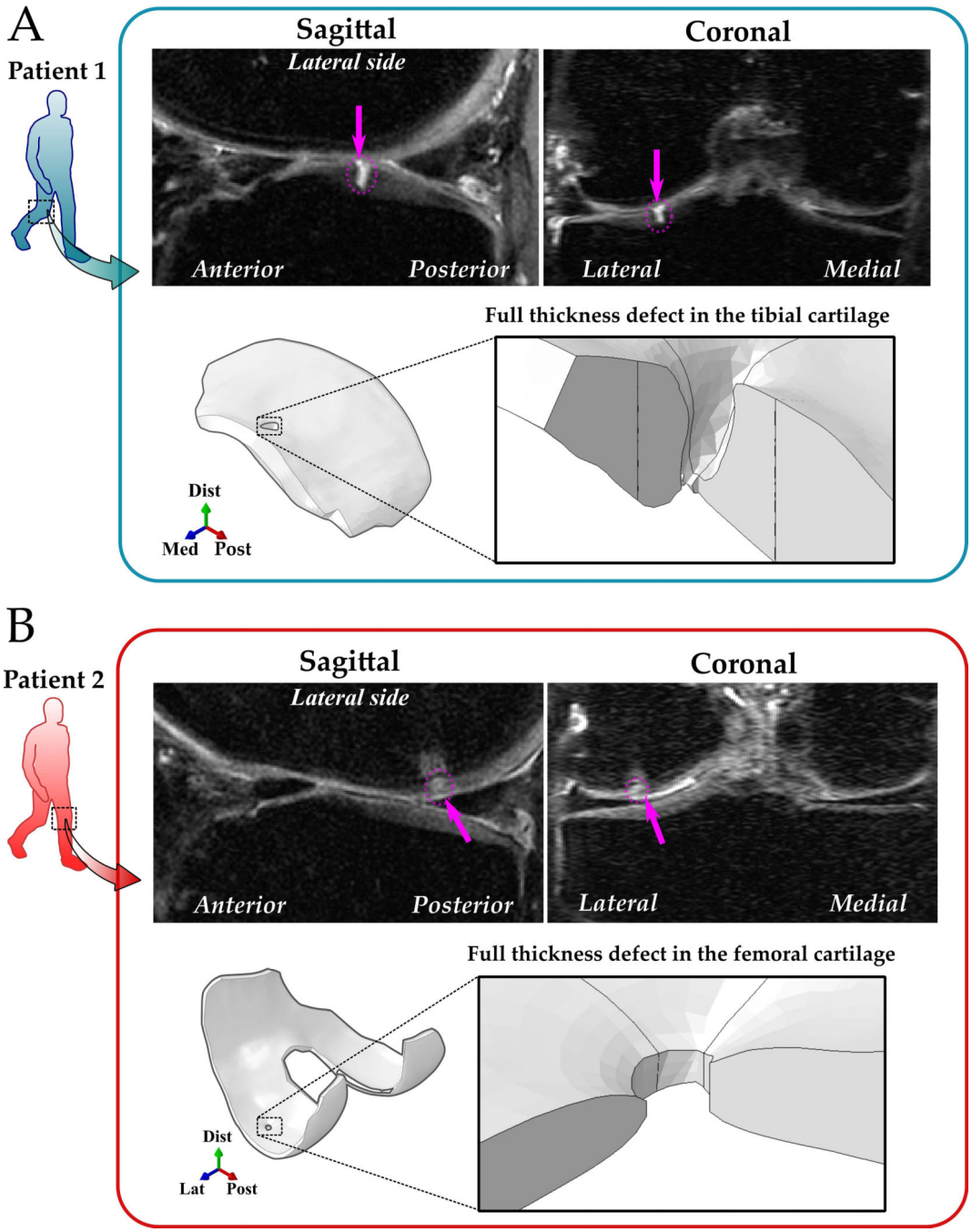

Figure 3.

Lesions in the articular cartilage identified in the MRI data at the 1-year follow-up time point (magenta dashed lines). These full thickness cartilage defects were especially considered during the segmentation process for developing numerical models for *Patient 1* (A) and *Patient 2* (B).

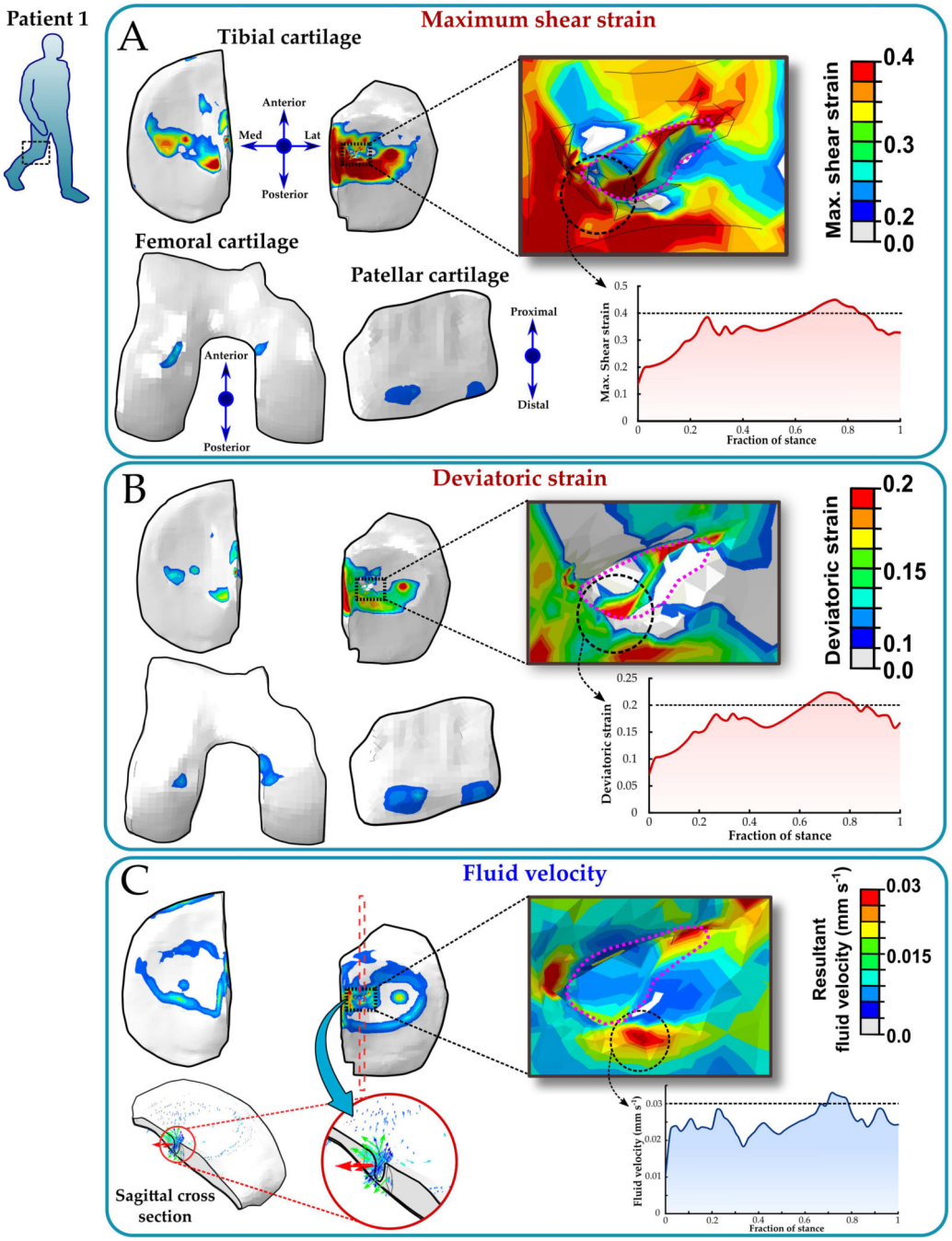

Figure 4.

(A) Maximum shear strain, (B) deviatoric strain, and (C) fluid flow velocity distributions for *Patient 1* at 75% of the stance phase of gait. For every studied mechanism, time-dependent changes of the maximum values as a function of the stance phase are shown. The thresholds to trigger adaptive responses of cartilage are indicated in the graphs with dashed lines.

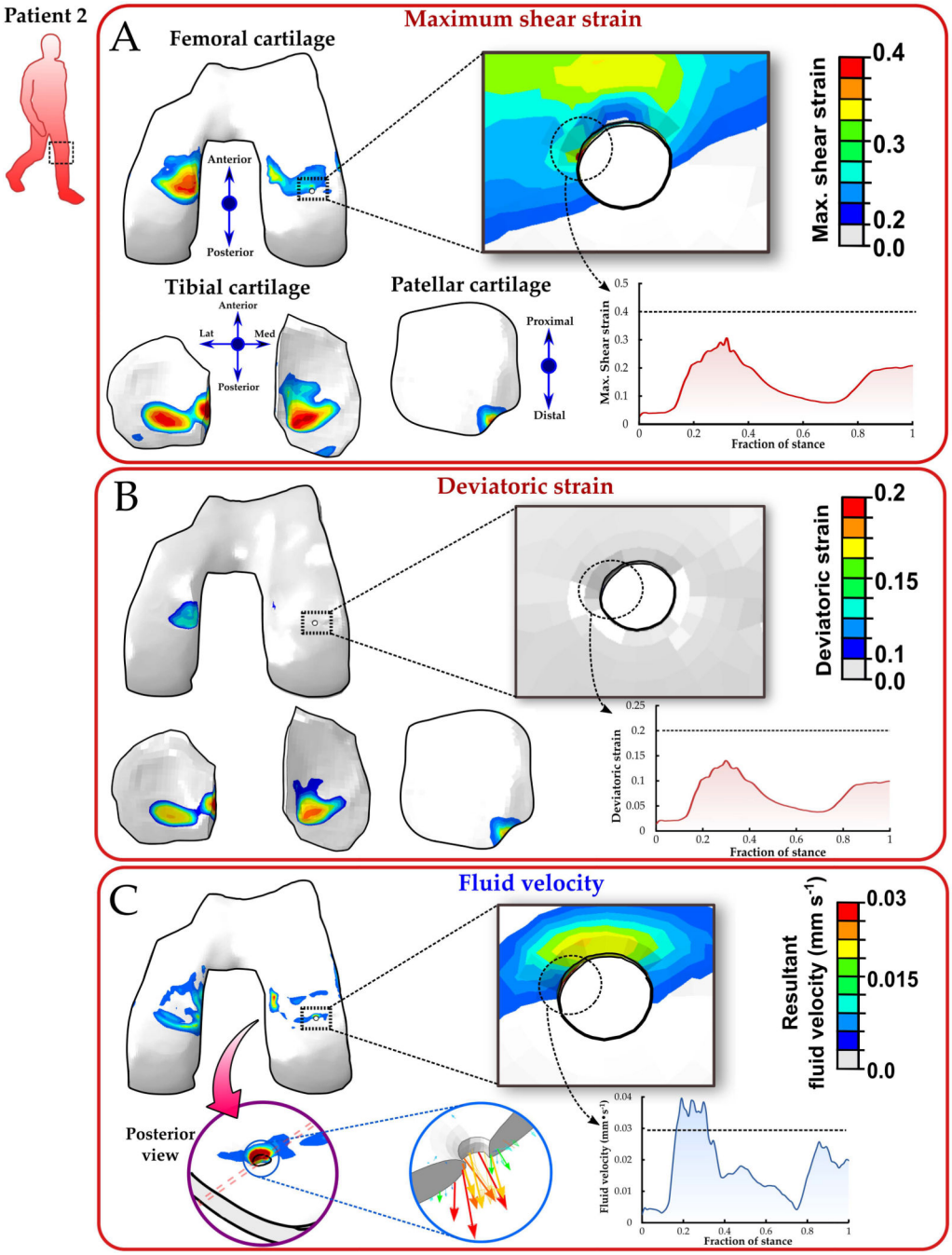

Figure 5.

(A) Maximum shear strain, (B) deviatoric strain, and (C) fluid flow velocity distributions for *Patient 2* at 35% of the stance phase of gait. For every studied mechanism, time-dependent changes of the maximum values as a function of the stance phase are shown. The thresholds to trigger adaptive responses of cartilage are indicated in the graphs with dashed lines.

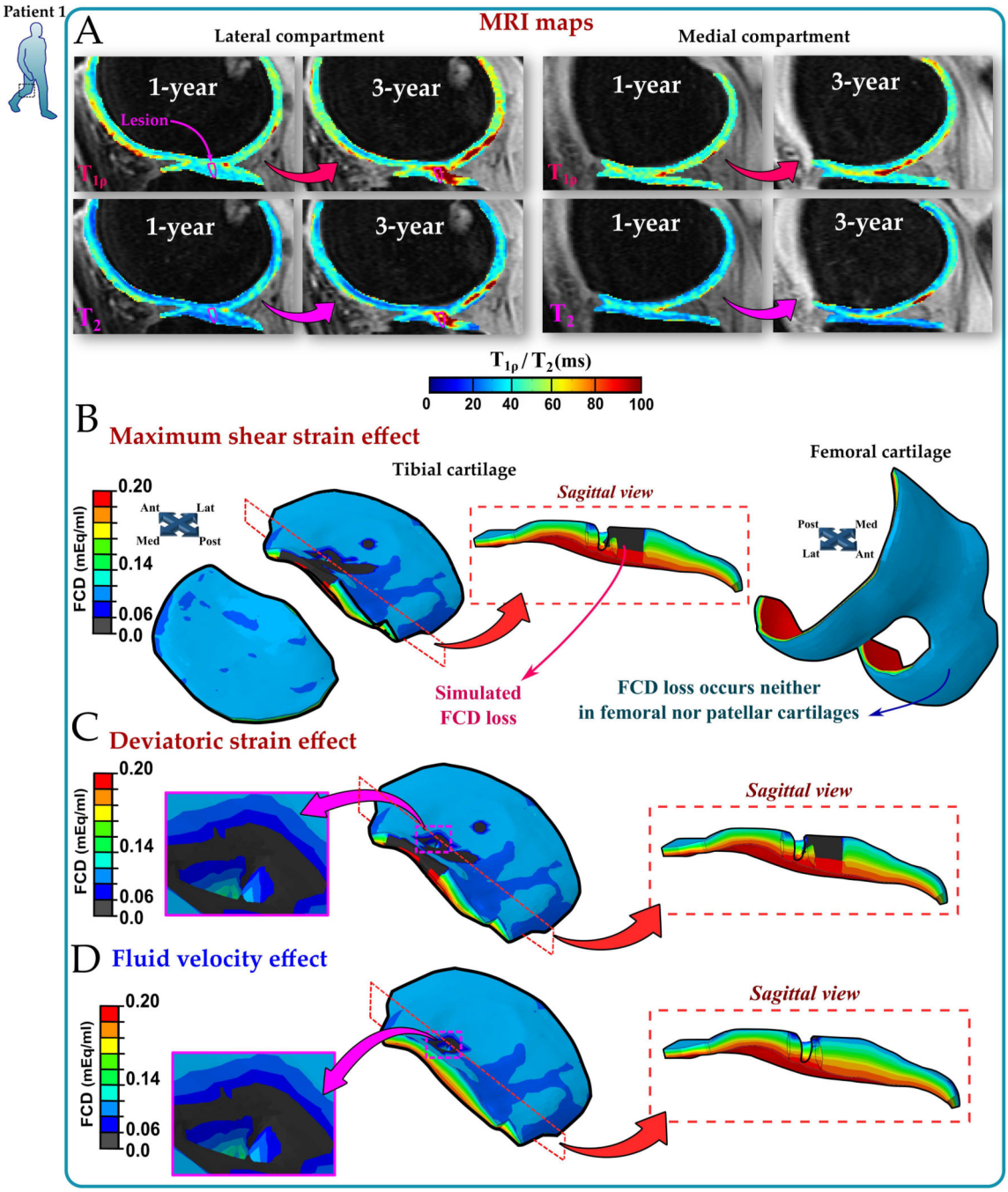

Figure 6.

(A) Sagittal $T_{1\rho}$ and T_2 map slices at both 1- and 3-year follow-up time points for the lateral and medial compartments of *Patient 1*. (B) FCD content distributions predicted by the models with maximum shear strain, (C) deviatoric strain, and (D) fluid flow driven adaptive mechanisms. FCD content reduced around the lesion and in the central surface of the lateral tibial cartilage when the adaptation algorithm was driven by the strain-based mechanism, while the fluid velocity mechanism revealed the FCD loss primarily around the cartilage defect.

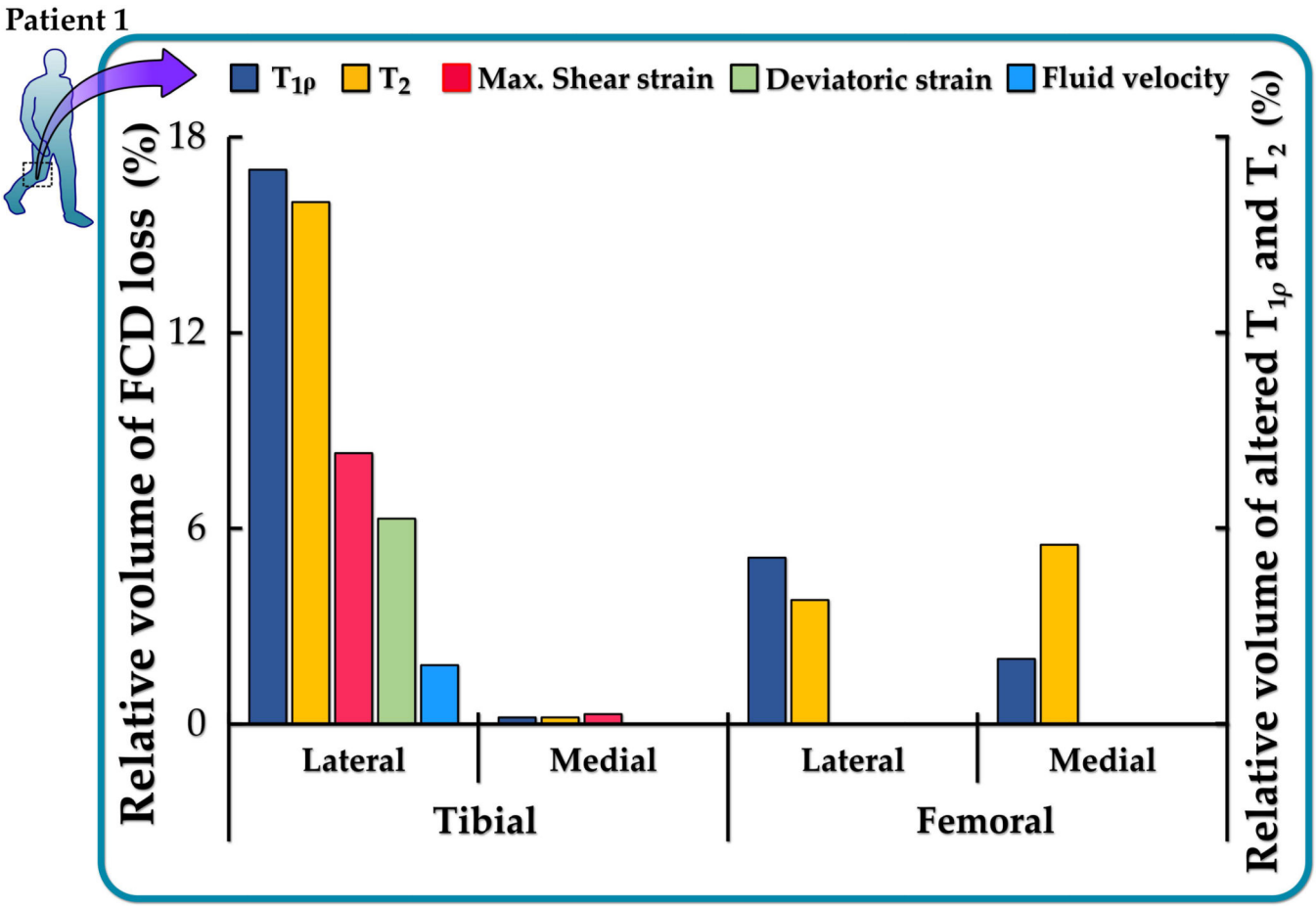

Figure 7.

Relative volumes of FCD loss, as predicted by each mechanism in the FE models, and altered $T_{1\rho}$ and T_2 relaxation times during the follow-up of *Patient 1*. The relative volume of FCD loss in the FE models was estimated as the volume of the elements associated with FCD loss in the last iteration, divided by the total volume of each compartment. The relative volume of cartilage with altered relaxation times was estimated by subtracting the calculated volume over the threshold of 60 ms at the 3-year time point from the volume at the 1-year time point, divided by the total volume of cartilage in the compartment.

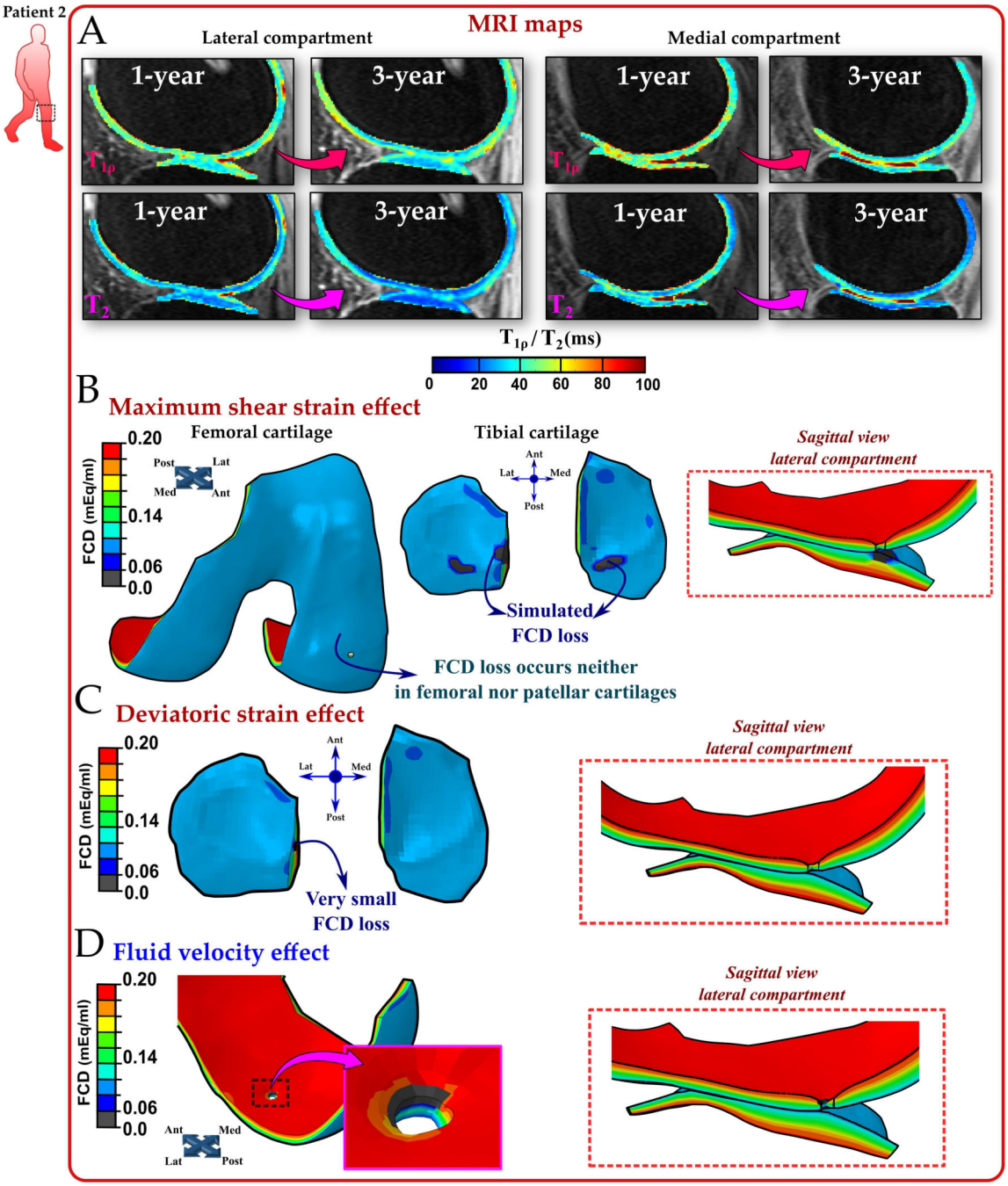

Figure 8.

(A) Sagittal $T_{1\rho}$ and T_2 map slices at both 1- and 3-year follow-up time points for the lateral and medial compartments in *Patient 2*. (B) FCD content distributions predicted by the models with maximum shear strain, (C) deviatoric strain, and (D) fluid flow driven adaptive mechanisms. FCD content reduced slightly in both compartments of the tibial cartilage when the adaptation algorithm was driven by the strain-based mechanism, while the fluid velocity mechanism showed a slight FCD loss around the lesion located in the lateral femoral cartilage.

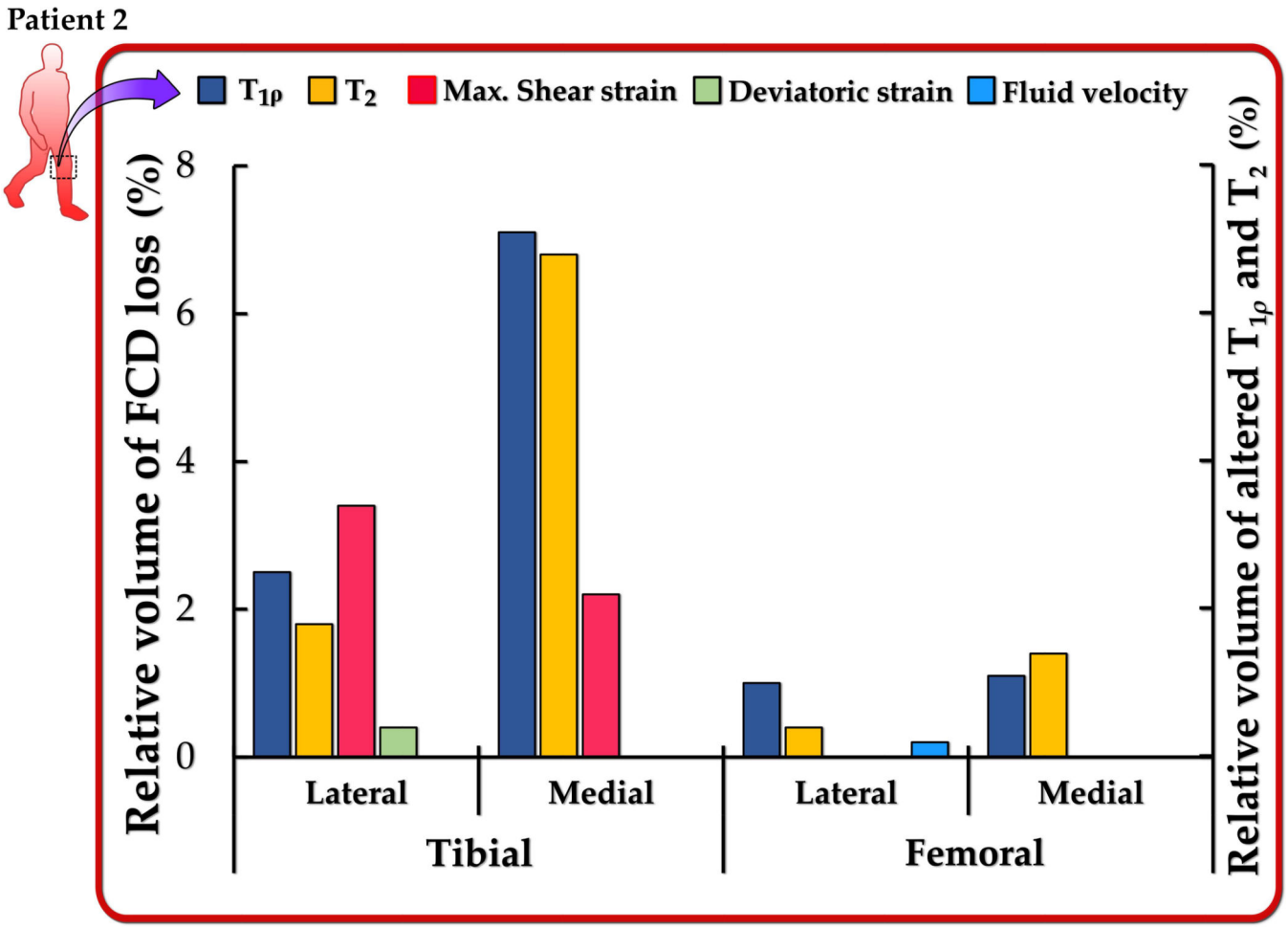

Figure 9.

Relative volumes of FCD loss, as predicted by each mechanism in the FE models, and altered $T_{1\rho}$ and T_2 relaxation times during the follow-up in *Patient 2.* The relative volume of FCD loss in the FE models was estimated as the volume of the elements associated with the FCD loss in the last iteration, divided by the total volume of each compartment. The relative volume of cartilage with altered relaxation times was estimated by subtracting the calculated volume over the threshold of 60 ms at the 3-year time point from the volume at the 1-year time point, divided by the total volume of cartilage in the compartment.

Table 1

Material parameters implemented for cartilages and menisci.

Material parameter	Femoral cartilage	Tibial cartilage	Patellar cartilage	Menisci
E_0 (MPa)	0.92 *	0.18 *	1.88 *	-
E_f (MPa)	-	-	-	28 ††
E_e (MPa)	150 *	23.6 *	597 *	-
η (MPa)	1062 *	1062 *	1062 *	-
E_{nf} (MPa)	0.215 *	0.106 *	0.505 *	0.5 *
k_0 (10^{-15} m^4/(Ns))	6 *	18 *	1.9 *	1.25 ††
ν_{nf}	0.15 **	0.15 **	0.15 **	0.36 ††
M	5.09 *	15.64 *	15.93 *	5.09
C	12.16 **	12.16 **	12.16 **	12.16 **
Composition				
n_{fl}	$0.8 - 0.15h$ **	$0.8 - 0.15h$ **	$0.8 - 0.15h$ **	0.72 ‡
c_{FCD} (mEq/ml)	$-0.1h^2+0.24h+0.056$ †	$-0.1h^2+0.24h+0.056$ †	$-0.1h^2+0.24h+0.056$ †	0.03 ‡‡
ρ_z	$20.6h^6 - 64.4h^5 +78.1h^4-45.9h^3+13.4h^2-1.6h +0.96$ †	$20.6h^6 - 64.4h^5 +78.1h^4-45.9h^3+13.4h^2-1.6h +0.96$ †	$20.6h^6 - 64.4h^5 +78.1h^4 -45.9h^3+13.4h^2-1.6h+0.96$ †	1

E_0=initial fibril network modulus, E_f=fibril network modulus, E_e=strain-dependent fibril network modulus, η=damping coefficient, E_{nf}=nonfibrillar matrix modulus, k_0=initial permeability, ν_{nf}=Poisson's ratio of the nonfibrillar matrix, M = exponential term for the strain-dependent permeability, C=ratio of primary to secondary collagen fibers, n_{fl} =depth-wise fluid fraction distribution, c_{FCD} =depth-wise fixed charge density distribution, ρ_z=depth-wise collagen distribution, h indicates normalized distance from the cartilage surface (surface = 0, bottom = 1).

* Julkunen et al.[47]

** Wilson et al.[24]

† Saarakkala and Julkunen.[48]

†† Dabiri and Li.[49]

‡ Makris et al.[50]

‡‡ Mow and Ratcliffe.[51]